GEODYNAMICS

10.1126/sciadv.1500360

Dislocation-accommodated grain boundary sliding as the major deformation mechanism of olivine in the Earth's upper mantle

Tomohiro Ohuchi,[1]* Takaaki Kawazoe,[1,2] Yuji Higo,[3] Ken-ichi Funakoshi,[3,4] Akio Suzuki,[5] Takumi Kikegawa,[6] Tetsuo Irifune[1,7]

Understanding the deformation mechanisms of olivine is important for addressing the dynamic processes in Earth's upper mantle. It has been thought that dislocation creep is the dominant mechanism because of extrapolated laboratory data on the plasticity of olivine at pressures below 0.5 GPa. However, we found that dislocation-accommodated grain boundary sliding (DisGBS), rather than dislocation creep, dominates the deformation of olivine under middle and deep upper mantle conditions. We used a deformation-DIA apparatus combined with synchrotron in situ x-ray observations to study the plasticity of olivine aggregates at pressures up to 6.7 GPa (that is, ~200-km depth) and at temperatures between 1273 and 1473 K, which is equivalent to the conditions in the middle region of the upper mantle. The creep strength of olivine deforming by DisGBS is apparently less sensitive to pressure because of the competing pressure-hardening effect of the activation volume and pressure-softening effect of water fugacity. The estimated viscosity of olivine controlled by DisGBS is independent of depth and ranges from $10^{19.6}$ to $10^{20.7}$ Pa·s throughout the asthenospheric upper mantle with a representative water content (50 to 1000 parts per million H/Si), which is consistent with geophysical viscosity profiles. Because DisGBS is a grain size–sensitive creep mechanism, the evolution of the grain size of olivine is an important process controlling the dynamics of the upper mantle.

INTRODUCTION

Anisotropic propagation of seismic waves has been observed in Earth's upper mantle, and this is attributed to the crystallographic preferred orientation (CPO) of olivine associated with mantle dynamics. The observed seismic anisotropy has been explained as likely being due to the deformation of olivine by CPO generating dislocation creep (*1*). This interpretation of dislocation creep as the dominant mechanism is derived from extrapolating laboratory data on olivine plasticity (*2*, *3*) at pressures below 0.5 GPa, which is much lower than asthenospheric upper mantle pressures (2 to 13 GPa). Diffusion creep may also partly contribute to the deformation of olivine in the upper mantle (*1*, *4*), whereas other possible mechanisms, such as dislocation-accommodated grain boundary sliding (DisGBS) and diffusion-accommodated grain boundary sliding, have been thought to play only minor roles in some limited circumstances such as in melt-bearing rocks (*5*) and fine-grained rocks (*6*), respectively. A recent study (*7*) proposed that the DisGBS may dominate the upper mantle flow on the basis of deformation experiments for olivine at a pressure of 0.3 GPa and temperatures to 1523 K. Development of CPO of olivine through DisGBS-controlled creep is significant (*8*); therefore, this could explain upper mantle seismic anisotropy. Nevertheless, most experimental investigations on the deformation of olivine have been limited to pressures below 0.5 GPa (*7*, *9*–*11*), requiring significant extrapolation for the interpretation of upper mantle deformation.

Developments in experimental techniques have expanded the pressure limit for the measurements of the plasticity of minerals toward deeper regions of the mantle, using the rotational Drickamar apparatus (*12*) or the deformation-DIA apparatus (*13*), combined with synchrotron in situ x-ray observations. A recent study on pure forsterite aggregates under nominally dry conditions at pressures up to 5.4 GPa using the latter apparatus showed that it is in large part dislocation creep and to a lesser extent diffusion creep contribute to the flow in the asthenospheric upper mantle, whereas DisGBS is negligible (*14*). However, the dominant deformation mechanism in the upper mantle needs to be carefully evaluated while considering iron-bearing olivine flow because the presence of iron in natural olivine has important effects on the flow law parameters, but its effects are different among the deformation mechanisms [dislocation creep: (*4*, *15*); diffusion creep: (*16*, *17*); DisGBS: (*18*)]. Moreover, it has been reported that the creep strength of dry olivine controlled by DisGBS (*13*) is 3 to 10 times smaller than that controlled by dislocation creep (*12*). Because DisGBS is expected to dominate the deformation of olivine at relatively low temperatures (for example, 1473 K) at a laboratory strain rate (for example, 10^{-5} s^{-1}) (*13*), we choose experimental temperatures (1273 to 1473 K) lower than the typical upper mantle temperatures. It has been reported that dislocation creep dominates the deformation of olivine at a laboratory strain rate at upper mantle temperatures and pressures (*12*). Although Hirth and Kohlstedt (*10*) discussed that DisGBS-controlled creep of olivine appears to be absent under hydrous conditions, the effect of water on DisGBS of olivine should also be clarified with deformation experiments under asthenospheric upper mantle conditions because the effects of water on the flow behavior of olivine have not been fully addressed at high pressures.

[1]Geodynamics Research Center, Ehime University, Matsuyama 790-8577, Japan. [2]Bayerisches Geoinstitut, University of Bayreuth, 95440 Bayreuth, Germany. [3]Japan Synchrotron Radiation Institute, Sayo, Hyogo 679-5198, Japan. [4]Research Center for Neutron Science and Technology, Ibaraki 319-1906, Japan. [5]Department of Earth and Planetary Materials Science, Graduate School of Science, Tohoku University, Sendai 980-8578, Japan. [6]Photon Factory, High Energy Accelerator Research Organization, Tsukuba 305-0801, Japan. [7]Earth-Life Science Institute, Tokyo Institute of Technology, Tokyo 152-8550, Japan.
*Corresponding author. E-mail: ohuchi@sci.ehime-u.ac.jp

RESULTS

We conducted uniaxial deformation experiments on olivine aggregates combined with synchrotron in situ x-ray observations at pressures of 1.5 to 6.7 GPa, temperatures of 1273 to 1473 K, and strain rates of 0.3×10^{-5} to 7.2×10^{-5} s^{-1} using a deformation-DIA apparatus

(table S1). Water content in the dry olivine aggregate is less than 20 parts per million (ppm) H/Si, and that in the wet olivine aggregate is 511 (TO-14 run) or 4071 ppm H/Si (M1301 and M1601 runs), respectively. In the deformation runs of the dry olivine aggregates and a wet olivine aggregate (TO-14), the change in dissolved water content was not significant. A significant water loss was observed in the M1301 and M1601 runs (that is, wet olivine aggregates) because the initial water content (4071 ppm H/Si) exceeds the solubility limit of water under the experimental conditions (see also Materials and Methods).

Microstructures

The recovered samples show protomylonitic or mylonitic microstructures with large porphyroclasts (30 to 80 μm) and recrystallized grains with grain sizes between 0.5 and 10 μm (Fig. 1 and fig. S1). Recrystallized grains were formed during the cold compression process followed by annealing (that is, before the deformation process) in the present experimental setup (*19*). Many grain boundaries are straight or slightly curved, and some lobate grain boundaries are also observed. The distribution of subgrain boundaries and dislocations is inhomogeneous, and larger porphyroclasts having grain sizes larger than 50 μm tend to have lower subgrain boundary densities and lower dislocation densities (Fig. 1). Most dislocations are straight or slightly curved, and they are not tangled with each other. Although the samples were deformed under high differential stress (for example, 355 to 708 MPa in the TO-24 sample: Fig. 1 and table S1), the dislocation density is significantly lower (for example, 3.7 μm^{-2} in the TO-24 sample) than that expected from the dislocation density piezometer for olivine (for example, 10 to 50 μm^{-2} for the TO-24 sample) (*20*).

The development (or absence) of CPO during sample deformation is one of the most important types of evidence to constrain the deformation mechanism (*21*). In most cases, the observed olivine CPO patterns are similar to each other in the present study (fig. S2). The [010] axes of olivine are preferentially subparallel to the direction of the axial differential stress. The [100] and [001] axes tend to form girdles perpendicular to the direction of the axial differential stress at high strains, though the concentration of the [100] and [001] axes is much weaker than that of the [010] axes. This fabric is consistent with that predicted by numerical simulations of the uniaxial compression of olivine having the dominant slip system of (010)[100] (*22*). From electron backscatter diffraction (EBSD) analyses on the lattice rotation around a tilt wall (fig. S1, E and F) and the transmission electron microscope (TEM) micrograph (fig. S3), activation of the (010)[100] slip system (and also the (100)[001] system) is supported, and thus, the development of A-type olivine fabric is expected under the present experimental conditions (see Supplementary Materials text for details) (*23*).

Mechanical data and flow laws

All the stress-strain curves obtained using five diffraction peaks (*hkl* = 021, 101, 130, 131, and 112) are shown in Fig. 2 and fig. S4. In many cases, quasi–steady-state creep strength was achieved at a strain of ε ~0.03,

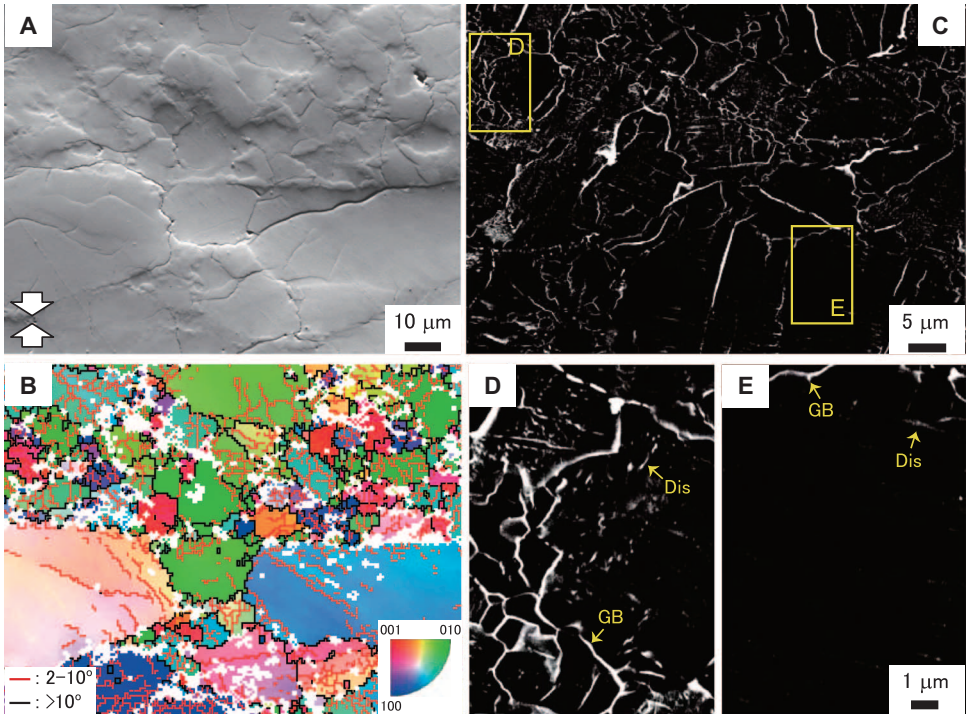

Fig. 1. Microstructures of deformed samples. (**A** and **B**) A forescattered electron (FSE) image (A) and an orientation map (B) of olivine in a deformed sample (TO-24). (A) and (B) were obtained at the same place in the sample. Large arrows in (A) represent the direction of the uniaxial compression. Uncolored points in (B) represent misindexed points. Red and black lines in (B) represent low-angle grain boundaries having 2 to 10° misorientation angles and grain boundaries having the misorientation angles greater than 10°, respectively. Wild spikes were removed and orientation data were extrapolated in (B). The orientation maps are colored by the relationship between the direction of uniaxial compression and olivine axes (blue: compression direction // [100]; green // [010]; red // [001]). (**C** to **E**) Backscattered electron (BSE) images showing heterogeneous distribution of dislocations in a deformed sample (TO-24). The internal-oxidation dislocation-decoration technique was adopted for the TO-24 sample. Bright lines show (sub-) grain boundaries (GB) or dislocations (Dis). Grains having many free dislocations and a dislocation-poor porphyroclast are observed in (D) and (E), respectively.

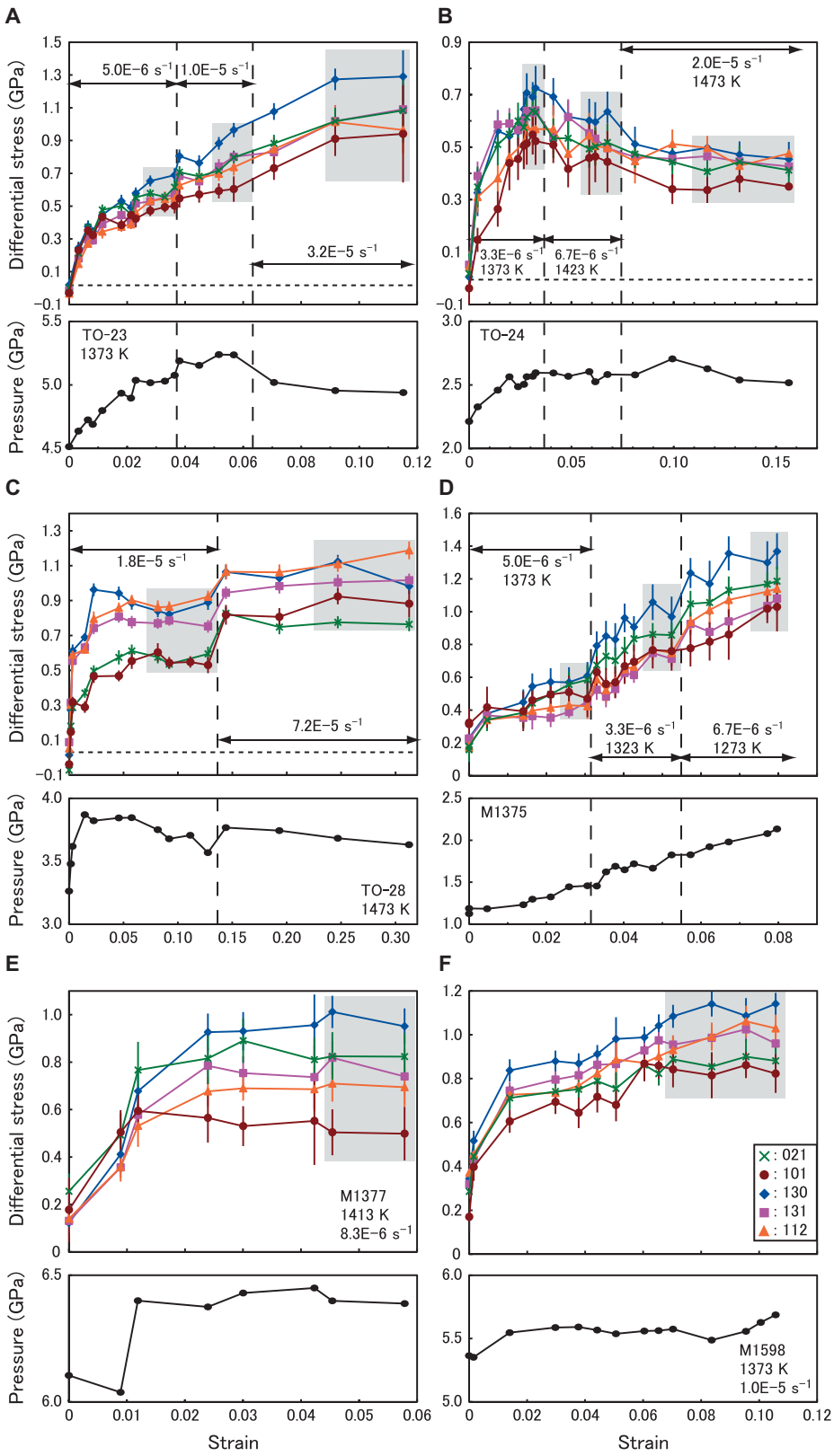

Fig. 2. Stress-strain records for dry olivine aggregates. The stress values were obtained from the five diffraction peaks of olivine (cross: 021; circle: 101; diamond: 130; square: 131; triangle: 112). The hatched areas indicate that the steady state was achieved in each deformation step. The change of pressure during the sample deformation is also shown.

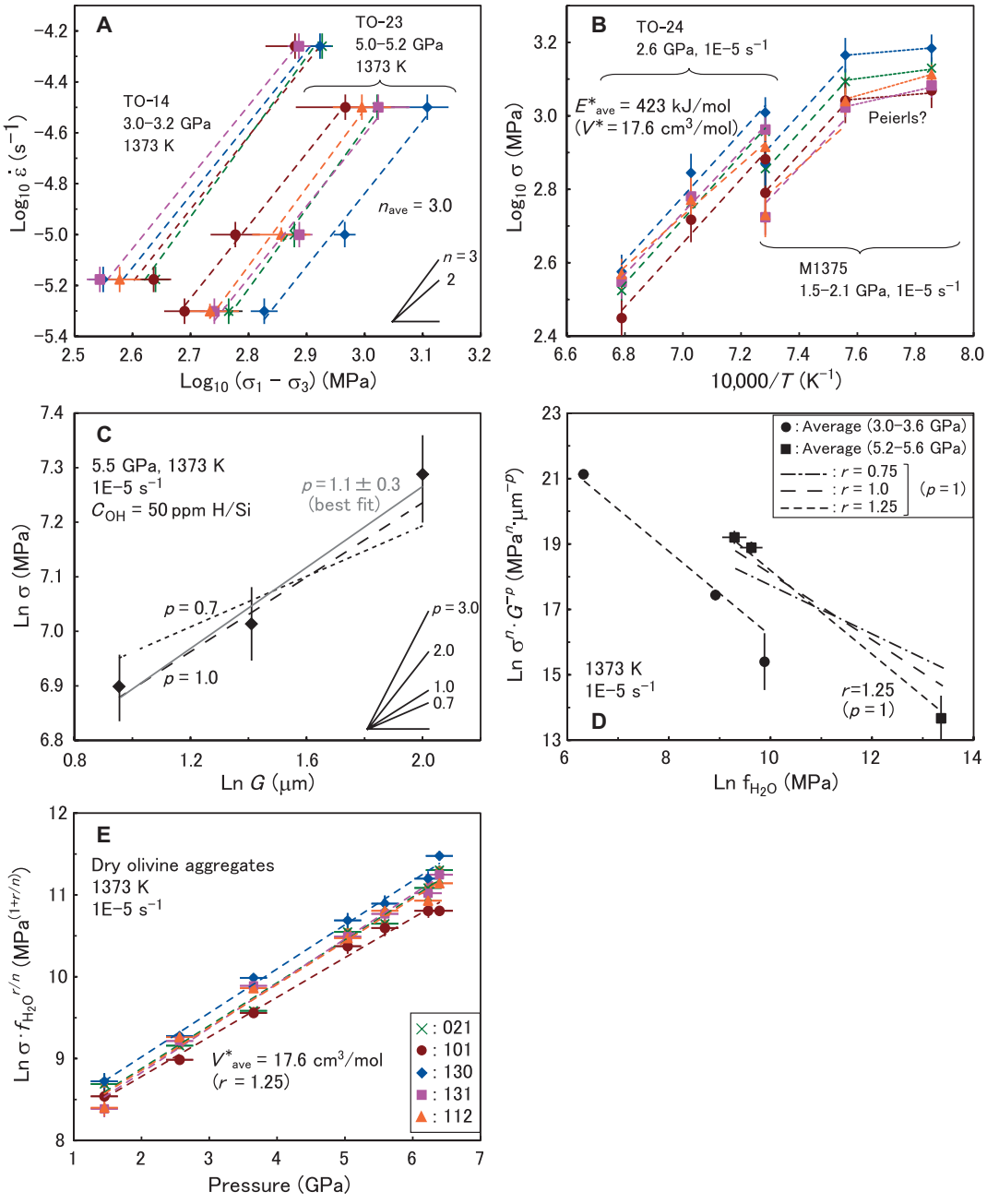

Fig. 3. Evaluation of flow law parameters for olivine aggregates. (**A**) Strain rate dependencies of steady-state creep strength (hereafter, strength) of olivine aggregates (dry: TO-23; wet: TO-14). The stress exponent *n* was obtained from this data set without any data normalization. (**B**) Strength of dry olivine aggregates plotted against inverse temperatures (TO-24 and M1375). Data was normalized to a strain rate of 10^{-5} s^{-1} using the *n*, and then the apparent activation enthalpy ($E^* + PV^*$) was obtained. After the determination of the activation volume V^* in (E), the activation energy E^* was obtained. (**C**) Grain size (*G*) dependence of the strength of dry olivine aggregates at 5.2 to 6.2 GPa and 1373 K (data from TO-23-step2, M1598-step1, and M1684). Data are normalized to the conditions of a uniform pressure (5.5 GPa), strain rate (10^{-5} s^{-1}), and water content (50 ppm H/Si) using the *n*, V^*, and water fugacity exponent $r = 1.25$ (see text). The data are best fit by the flow law with the grain size exponent $p = 1.1 \pm 0.3$ (gray solid line). The best-fit lines assuming reported values of *p* are also shown ($p = 0.7$: short-dashed; 1.0: long-dashed). (**D**) Water fugacity sensitivity of the strength of olivine at 3.0 to 3.6 GPa (circles: data from TO-14-step1, TO-28-step1, and M1301-step1) and at 5.2 to 5.6 GPa (squares: data from TO-23-step2, M1598-step1, and M1601-step1) in the case of $p = 1$. The data are normalized to a strain rate of 10^{-5} s^{-1} and a temperature of 1373 K. The best-fit lines assuming theoretical values of *r* are also shown ($r = 0.75$: dot-dashed; 1.0: long-dashed; 1.25: short-dashed). Both of the data sets are best fit by the flow law with $r = 1.25$. (**E**) Pressure dependency of the strength of dry olivine aggregates in the case of $r = 1.25$. The strength is corrected for water fugacity effects (that is, $f_{H_2O}^{r/n}$). Data are normalized to the conditions of 1373 K and a strain rate of 10^{-5} s^{-1}. The grain size effect on strength is not corrected because the determined value of *p* has a significant uncertainty in this study. The strength was obtained from the five diffraction peaks of olivine (cross: 021; circle: 101; diamond: 130; square: 131; triangle: 112). The dashed lines represent the best fits defined as the flow law. The averaged best-fit values of flow law parameters (shown by subscript "ave") are also shown.

although higher strains up to 0.08 were sometimes required for the achievement of a quasi–steady-state flow. In many runs, the confining pressure gradually increases at a constant strain rate and temperature because of shrinking of the pressure medium during the deformation process. Pressure change during a deformation step was within 0.4 GPa (except for the pressure change at the beginning of deformation), resulting in fluctuations in steady-state creep strength (within the range of ±0.05 GPa: estimated by using the obtained value of the activation volume).

Plastic flow of minerals at high temperatures is commonly described as shown below

$$\dot{\varepsilon} = A\frac{\sigma^n}{G^p} f_{H_2O}^r \exp\left(-\frac{E^* + PV^*}{RT}\right) \quad (1)$$

where $\dot{\varepsilon}$ is strain rate, A is a material-dependent parameter, σ is differential stress, n is the stress exponent, G is grain size, p is the grain size exponent, f_{H_2O} is water fugacity, r is the water fugacity exponent, E^* is the activation energy, P is pressure, V^* is the activation volume, R is the gas constant, and T is temperature. Flow law parameters for olivine aggregates were obtained from the experimental data using a linear least-square fitting method (table S2). The slopes of the lines in Fig. 3 (A and B) show that the dominant creep mechanism of olivine aggregates is unique at temperatures of 1323 to 1473 K [see Eq. (1)]. The averaged values of stress exponent n and activation energy E^* were 3.0 ± 0.3 kJ/mol and 423 ± 56 kJ/mol, respectively. The quasi–steady-state creep strength becomes insensitive to temperature at lower temperatures (for example, 1273 K), suggesting a temperature-induced transition of the creep mechanism to the Peierls mechanism (Fig. 3B) (*9*). A significant grain size dependence on the creep strength of olivine was observed at 5.5 to 6.2 GPa and 1373 K, and its dependence is best fit by the flow law with grain size exponent p = 1.1 ± 0.3. The best-fit value is close to a theoretical value of grain size exponent p = 1 (*24*), rather than a reported value of 0.7 for olivine (Fig. 3C) (*7*). Here, we use the theoretical value of p (=1) as the flow law parameter instead of the best-fit value, because the best-fit value has a significant uncertainty. Using a data set obtained at a wide range of water fugacities, we evaluated the water fugacity dependency of stress in Fig. 3D. Adopting theoretical values of water fugacity exponent r for olivine (=0.75, 1, or 1.25) (*11*, *25*), our results are best fit by the flow law with r = 1.25 in the case of p = 0.7 or 1 (note that an unrealistic value of r higher than 1.25 was expected if we assume p = 2 to 3). From the pressure dependency of the stress on the dry olivine aggregates, we obtained an averaged activation volume of V^* = 17.6 ± 0.8 cm^3/mol (Fig. 3E).

The flow law parameters obtained support our conclusion that the deformation of olivine is controlled by DisGBS. The parameters are consistent with a theoretical model for DisGBS in which n = 3 and p = 1 (*24*). Our value of the activation energy (E^* = 423 ± 56 kJ/mol) is close to the activation energy for DisGBS of dry olivine (445 ± 20 kJ/mol) (*7*) and is between the activation energies for dislocation creep (530 ± 4 kJ/mol) and diffusion creep (375 ± 50 kJ/mol) of dry olivine (*10*). The olivine flow law we obtained is best described with the following relation (strain rate $\dot{\varepsilon}$ in s^{-1}; grain size G in m; stress σ, pressure P, and water fugacity f_{H_2O} in MPa)

$$\dot{\varepsilon} = 10^{-4.89\pm0.24}\frac{\sigma^{3.0\pm0.3}}{G} f_{H_2O}^{1.25} \exp\left(-\frac{423 \pm 56\,\text{kJ/mol} + P \times 17.6 \pm 0.8 \times 10^{-6}\text{m}^3\text{/mol}}{RT}\right) \quad (2)$$

DISCUSSION

Steady-state creep strength, which is normalized at a fixed temperature and strain rate, is plotted against pressure in Fig. 4. Creep strength of olivine aggregates having various water contents (up to 3681 ppm H/Si) obtained in the present study is well reproduced by Eq. (2). The dependency of the creep strength of olivine aggregates controlled by DisGBS on pressure is apparently weak because of a combination of the activation volume of 17.6 cm^3/mol and a strong effect caused by the water fugacity (r = 1.25). The calculated creep strength of dry olivine controlled by the dislocation creep is too high to account for our data. Note that DisGBS creep strength of a water-rich olivine aggregate (that is, 3681 ppm H/Si) is much lower than the lower limit of creep strength of olivine controlled by wet dislocation creep (that is, the water-saturated case). The strength contrast between dry dislocation creep and DisGBS is quite small at 0.3 GPa (*7*), although it

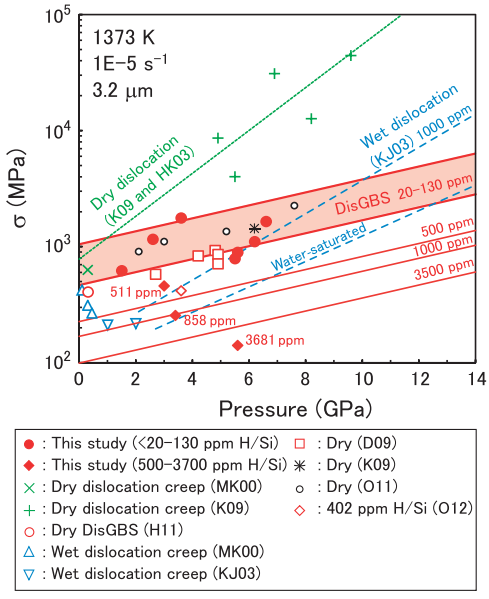

Fig. 4. Pressure dependency of strength of olivine aggregates. All data are normalized to an axial strain rate of 10^{-5} s^{-1}, a temperature of 1373 K, and a grain size of 3.2 μm (that is, the average value of the mean grain size of dry olivine in this study). Large solid circles and solid diamonds represent the strength of dry olivine aggregates (<20 to 130 ppm H/Si) and wet olivine aggregates (500 to 3700 ppm H/Si: water content is shown near the symbols), respectively. Other symbols represent the data from previous studies. Crosses: dry olivine aggregates controlled by dislocation creep [K09 (*12*), MK00 (*11*)]; open large circle: dry olivine aggregates controlled by DisGBS (*7*); open triangles: wet olivine aggregates controlled by dislocation creep [KJ03 (*25*), MK00 (*11*)]. The dominant creep mechanism is unknown in the case of other symbols (the grain size effect on stress is not corrected). Open squares: dry olivine aggregates presumed to be controlled by DisGBS (D09) (13); star: a dry olivine aggregate (K09) (*12*); open small circles: dry olivine aggregates (O11) (*26*); open diamond: an olivine aggregate having 402 ppm H/Si of water (O12) (*19*). Red lines represent the strength of olivine aggregate controlled by DisGBS shown in Eq. (2) (thick lines with a hatched area: 20 to 130 ppm H/Si; thin lines: 500 to 3500 ppm H/Si of water in olivine). The green dotted line represents the strength of dry olivine aggregates controlled by dislocation creep [K09 (*12*) and HK03 (*10*)]. Blue dashed lines represent the strength of wet olivine aggregates controlled by wet dislocation creep [KJ03 (*25*)] (1000 ppm H/Si and water-saturated cases are considered).

drastically increases with pressure (Fig. 4). The creep strength of dry olivine aggregates in the present study is consistent with that reported by several previous studies (*13*, *26*).

To determine which creep mechanism controls the upper mantle flow, we calculated deformation mechanism maps as a function of stress and grain size under representative upper mantle conditions (Fig. 5). In the calculation, we used olivine flow laws reported in the present study (DisGBS) and in previous studies (*7*, *10*, *12*, *14*, *17*, *19*, *25*). For water-rich conditions, we adopted 1000 to 3000 ppm H/Si (that is, typical water contents in the water-rich upper mantle) (*27*) for all flow

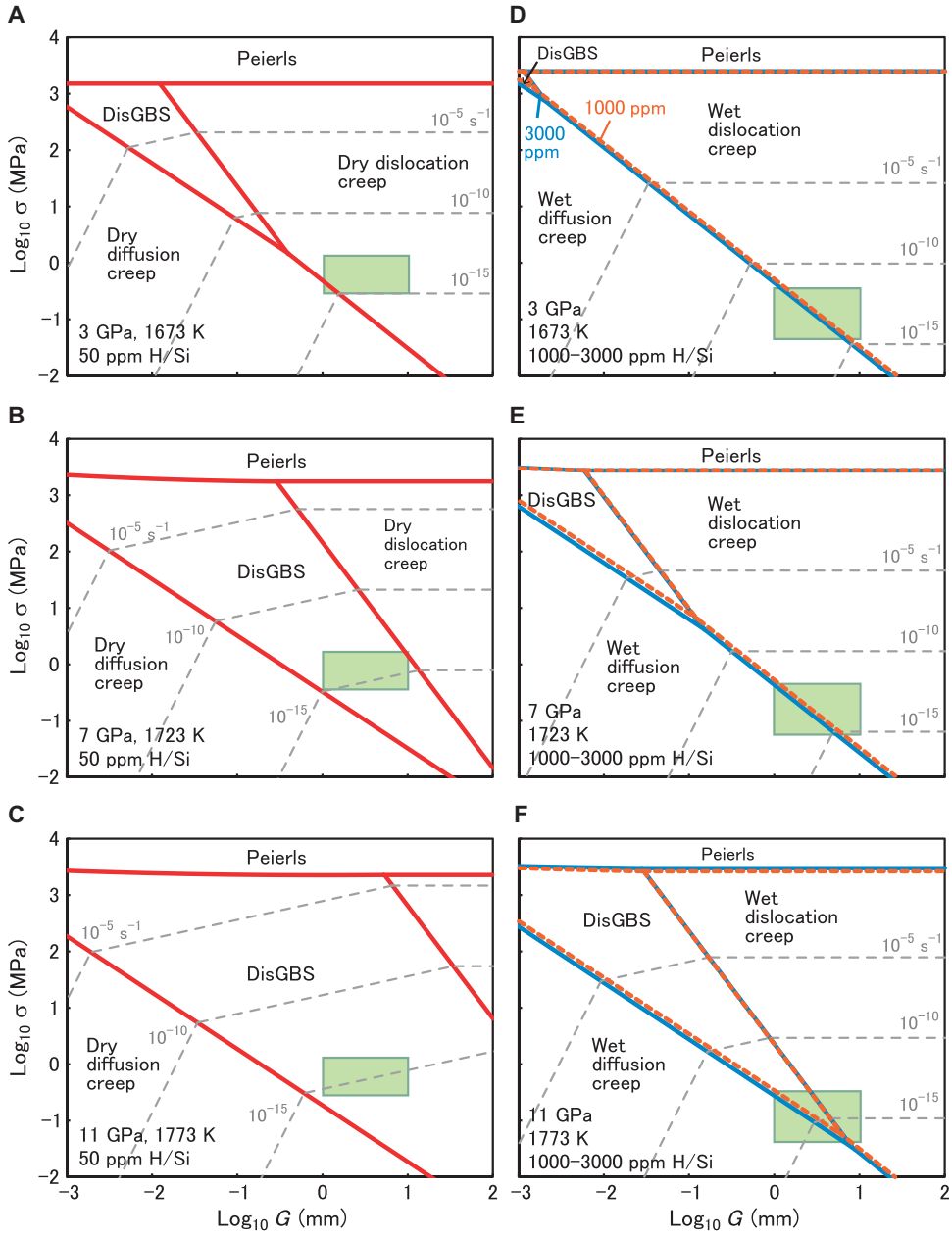

Fig. 5. Deformation mechanism maps for olivine on the axes of differential stress versus grain size. (**A** to **F**) Calculation was made for the case of olivine having water contents of (A to C) 50 ppm H/Si (that is, dry) and (D to F) 1000 to 3000 ppm H/Si (that is, wet). Pressures of 3 to 11 GPa and temperatures of 1673 to 1773 K are assumed for the calculations (that is, corresponding to typical asthenospheric upper mantle conditions). The lines represent the boundaries between two deformation mechanisms. The boundaries were calculated from the flow laws of olivine for dislocation creep, diffusion creep, the Peierls mechanism, and DisGBS (see table S3 for references). Red solid lines, orange dotted lines, and blue solid lines represent the boundaries for the case of 50, 1000, and 3000 ppm H/Si, respectively. The green hatched area represents typical conditions of the asthenospheric upper mantle. The range of grain size is from the data set of olivine in peridotite xenoliths beneath the continental extension zones and cratons (*50*). The range of stress is based on the viscosity-depth profiles in the upper mantle estimated by Kohlstedt and Hansen (*28*) and this study (see text for details). The gray dashed lines represent the contours of strain rates.

law calculations. The deformation mechanism maps for dry upper mantle conditions (50 ppm H/Si: Fig. 5, A to C) show that the viscosity of the dry upper mantle is controlled by DisGBS of olivine at high pressures (≥7 GPa), whereas contributions of dislocation and diffusion creep to mantle flow are limited only to the shallow upper mantle (Fig. 5A). DisGBS is more effective at a larger strain rate (that is, a larger stress) and a smaller grain size. As shown in Fig. 5 (D to F), viscosity of the water-rich mantle (for example, 1000 to 3000 ppm H/Si) is dominantly controlled by dislocation creep or diffusion creep of wet olivine, and the contribution of DisGBS to wet upper mantle flow is limited in the deeper part of the upper mantle (≥11 GPa: Fig. 5F).

Figure 6 shows the viscosity-depth profiles in the upper mantle based on the present results, where a constant stress and a constant rate of viscous dissipation (that is, constant $\dot{\varepsilon}\sigma$) are assumed (*10*). A constant stress or a constant viscous dissipation rate that produces the desired average strain rate [that is, 10^{-15} s^{-1} in the asthenospheric upper mantle (100 to 400 km depth)] was adopted for each calculation [for example, (*28*)] (Fig. 6). The viscosity profiles show strong depth dependencies ranging from $10^{18.5}$ to $10^{22.7}$ (dry) and from $10^{18.5}$ to $10^{20.9}$ Pa·s (wet) in the case of dislocation creep–controlled flow. In contrast, the upper mantle is estimated to have relatively constant viscosities in a limited range of $10^{20.1}$ to $10^{20.7}$ Pa·s (in the case of 50 ppm H/Si of water) or $10^{19.6}$ to $10^{20.1}$ Pa·s (in the case of 1000 ppm H/Si of water) at depths greater than ~100 km when the constant stress flow is controlled by DisGBS (Fig. 6A). The depth dependency of viscosity is significantly reduced in the case of the constant viscous dissipation rate model (within two orders of magnitude; Fig. 6B). In Fig. 6 (A and B), the case of DisGBS with 50 ppm H/Si of water is harmonious with the viscosity-depth profiles derived from geophysical observations on post-glacial rebound (*29*–*31*) and those from observations of the geoid, topography, and plate velocities (*32*), where viscosities in the upper mantle are estimated to be 10^{20} to 10^{21} Pa·s and are insensitive to depth. The range of viscosities in the case of DisGBS with 1000 ppm H/Si is marginally consistent with the lower limit of the geophysical observations on post-glacial rebound. Thus, we conclude that DisGBS-controlled flow of olivine with 50 to 1000 ppm H/Si of water best describes the observed viscosity profiles in the upper mantle.

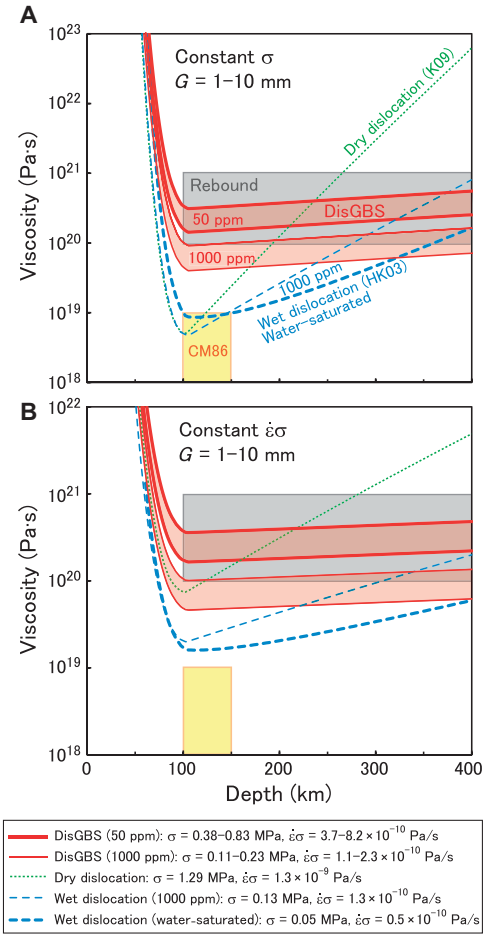

Fig. 6. Depth dependency of the viscosity of olivine. The dominant deformation mechanism is assumed to be DisGBS (red solid curves with red hatched areas; thick: 50 ppm H/Si; thin: 1000 ppm H/Si) or wet dislocation creep (blue dashed curves; thin: 1000 ppm H/Si; thick: water-saturated). Viscosity of olivine controlled by dry dislocation creep is also shown for reference (green dotted curves). (**A** and **B**) A constant stress and a constant viscous dissipation rate are assumed for each viscosity profile, respectively (used values are summarized in the box). Geotherms below the 50 million-year-old oceans and mantle adiabat (*51*, *52*) are used for the calculation. The gray and yellow hatched areas represent the ranges of upper mantle viscosity estimated from geophysical observations on post-glacial rebound (*29*–*31*) and the geoid (CM86) (*34*), respectively.

In contrast, the upper mantle is estimated to have relatively constant viscosities in a limited range of $10^{20.1}$ to $10^{20.7}$ Pa·s (in the case of 50 ppm H/Si of water) or $10^{19.6}$ to $10^{20.1}$ Pa·s (in the case of 1000 ppm H/Si of water) at depths greater than ~100 km when the constant stress flow is controlled by DisGBS (Fig. 6A). The depth dependency of viscosity is significantly reduced in the case of the constant viscous dissipation rate model (within two orders of magnitude; Fig. 6B). In Fig. 6 (A and B), the case of DisGBS with 50 ppm H/Si of water is harmonious with the viscosity-depth profiles derived from geophysical observations on post-glacial rebound (*29*–*31*) and those from observations of the geoid, topography, and plate velocities (*32*), where viscosities in the upper mantle are estimated to be 10^{20} to 10^{21} Pa·s and are insensitive to depth. The range of viscosities in the case of DisGBS with 1000 ppm H/Si is marginally consistent with the lower limit of the geophysical observations on post-glacial rebound. Thus, we conclude that DisGBS-controlled flow of olivine with 50 to 1000 ppm H/Si of water best describes the observed viscosity profiles in the upper mantle.

A comparison of the laboratory data on the electrical conductivity of olivine with geophysical observations suggests that the typical oceanic asthenosphere contains 1500 ppm H/Si of water, whereas the water content in the continental upper mantle is less than 150 ppm H/Si (*33*). Because the geophysically constrained viscosity profiles based on the post-glacial rebound usually represent those of the subcontinental upper mantle, the viscosity profiles for dry olivine (Fig. 6) would be applicable to such regions. A geophysical estimate based on the geoid data (*34*) showed that the viscosity of the shallow oceanic upper mantle is less than 10^{19} Pa·s. Figure 6 suggests that the low viscosity of the oceanic upper mantle is partly attributed to the flow of wet olivine (1000 ppm H/Si or higher), taking into account the relatively high water content in this region of the upper mantle (*33*).

In many of the previous numerical models of upper mantle dynamics such as the initiation of subduction, plate tectonics, and mantle convection, dislocation creep of dry olivine has been assumed to be the dominant flow mechanism (*35*, *36*). However, our results show that assuming the dislocation creep of dry olivine would significantly overestimate deep upper mantle viscosity by ~10 to 10^2 times. Such an estimate of upper mantle viscosity leads to the highly unlikely conclusion that the deep upper mantle may have a viscosity of ~10^{23} Pa·s, which corresponds to the upper bound of the lower mantle viscosity (10^{21} to 10^{23} Pa·s) (*29*–*31*). The dynamics of the upper mantle should also be reevaluated using our new flow law for DisGBS of olivine obtained under realistic upper mantle conditions.

MATERIALS AND METHODS

The starting materials of an olivine aggregate were prepared from powdered San Carlos olivine (Fo_{90}). Mixtures of powdered San Carlos olivine + 8 volume % pyroxenes (4 volume % clinopyroxene + 4 volume % orthopyroxene) and San Carlos olivine + 8 volume % orthoenstatite were used for the synthesis of the starting materials for the TO-14 and M1684 runs, respectively. The fine-grained powder was placed into a

nickel capsule and was sintered at 2 to 4 GPa and 1273 to 1373 K for 1.5 hours using a Kawai-type multi-anvil apparatus at Ehime University. To remove water dissolved in the olivine aggregates, some of the hot-pressed samples were fired at 0.1 MPa and 1170 K under reducing conditions (f_{O2} ~10^{-16} bars) for up to 6 hours. The average grain sizes of olivine in the hot-pressed samples are 63, 13, and 8 μm for all runs (except for the TO-14 and M1684 runs), TO-14 runs, and M1684 runs, respectively. Because volume fraction of pyroxenes is 8 volume % in the starting materials for TO-14 and M1684 runs, sample deformation in the runs is almost entirely controlled by olivine (*37*). The hot-pressed sample was core-drilled with a diameter of 1.2 mm and a length of 1.2 or 1.5 mm.

Deformation experiments were performed using a deformation-DIA apparatus (D-CAP) at the AR-NE7A beamline of the Photon Factory or the deformation-DIA apparatus (SPEED-Mk.II) at the BL04B1 beamline at SPring-8. Two of the four sliding blocks on the downstream side have a conical x-ray path (maximum 2θ angle ~10°). The MA-6-6 system with 4- or 5-mm truncated edge lengths for the second-stage anvils was adopted for the experiments. Two x-ray–transparent anvils, which were made of cubic boron nitride, were used as the second-stage anvils on the downstream side. The anvil guide was made of engineering plastic (columns along x-ray path) and stainless steel (other parts) (*38*). Two different types of cell assembly [4–6.5 type: for TEL4mm anvils (fig. S5); 5–7 type (*19*): for TEL5mm anvils] were used in the experiments. A semi-sintered cobalt-doped magnesia [(Mg, Co)O] cube with an edge length of 6.5 mm (for the 4–6.5 type cell) or 7 mm (for the 5–7 type cell) was used as the pressure medium. A graphite heater was located at the inner bore of a tubular $LaCrO_3$ thermal insulator. Copper and molybdenum electrodes, hard alumina pistons, and machinable alumina rods were placed along the direction of the axial differential stress (σ_1-σ_3). Two x-ray–transparent rods, which were made from a mixture of amorphous boron and epoxy, were placed along the x-ray path in the pressure medium. A cored sample was placed into a palladium-silver (Pd75%-Ag25%) capsule and then sandwiched by two pistons made of hard alumina or single-crystal diamond to keep the dissolved water content constant during the experiment. Two platinum strain markers, with a thickness of 20 μm, were placed between the sample and the pistons. The palladium-silver capsule was surrounded by magnesia (4–6.5 type) or hexagonal boron nitride sleeves (5–7 type).

Procedures for the in situ deformation experiments are based on those in our previous studies (*19*). The main ram load was first raised to the desired value (up to 0.5 MN) at a rate of 0.3 MN/hour (in press load) by operating the main ram of the deformation-DIA apparatus. Shortening of the samples (5 to 10%) was observed during cold compression at room temperature. Temperature was increased at a rate of ~25 K/min. After the temperature reached the desired value, the sample was annealed for 0.5 hour, and then the upper and lower anvils were advanced at a constant rate by operating the deformation rams. Temperature was monitored by a $W_{97}Re_3$-$W_{75}Re_{25}$ thermocouple placed along one of the diagonal directions of the cubic pressure media. Temperatures at the center of the samples were estimated from the temperatures monitored by a thermocouple using a calibration line between the temperatures at the hot junction of the thermocouple and the central part of the sample. The temperature gradient between the central part and the edge of the sample was less than 50 K (*39*).

Axial differential stress and generated pressure were measured by using the radial diffraction of monochromatic x-rays (energy, 51 keV). Two-dimensional x-ray diffraction patterns were taken by using an imaging plate or a 2048 × 2048–pixel MAR-CCD camera (with 5 to 12 min of exposure time). The two-dimensional digitalized diffraction pattern was integrated to a one-dimensional profile (angle step of 10°), and the peak positions were semiautomatically determined at a certain azimuth angle using IPAnalyzer and PDIndexer software (*40*). The stress magnitude was calculated on the basis of the following equation (*41*)

$$d_{hkl} = d^0_{hkl}\left[1 + \frac{\sigma}{6M}\left(1-3\cos^2\psi\right)\right] \quad (3)$$

where d_{hkl} is the d-spacing measured at an azimuth angle ψ, d^0_{hkl} is the d-spacing under hydrostatic pressures, M is an appropriate shear modulus for a given crystal orientation [hkl], and σ is the axial differential stress. The value of M was calculated from olivine single crystal elasticity data (*42*, *43*). The values of σ and d^0_{hkl} were calculated by fitting the obtained values of d_{hkl} to Eq. (3). The uncertainty of the stress results from the deviation of the obtained values of d_{hkl} from the best-fit curve of Eq. (3). Pressure was determined from the calculated values of d^0_{hkl} using the equation of state of olivine (*44*). The analysis was carried out for five diffraction peaks of olivine (hkl = 021, 101, 130, 131, and 112). Representative x-ray diffraction patterns are shown in fig. S6. The strain [that is, $\varepsilon = -\ln(l/l_0)$, where l_0 is the initial length of the sample just before the operation of the deformation rams, and l is the length of the sample during deformation] of a sample was measured by the distance between two platinum strain markers that was monitored by in situ monochromatic x-ray radiography (fig. S7). The uncertainty in the strain rate, which resulted from the shape of the strain markers, was within 10%.

The recovered samples were cut with a low-speed saw. Polished surfaces of the samples were etched by dilute hydrofluoric acid to enhance the visibility of the grain boundaries and to evaluate the mean grain size. BSE and FSE images of the polished surfaces of the recovered samples were acquired at magnifications varying between ×50 and ×3000 by using a JEOL JSM-7000F field emission scanning electron microscope (FE-SEM). Grain boundary maps (that is, outline of grain boundaries) were obtained from an FSE image of the etched sample, and then diameters of the circles having the same area as individual grains were measured as the grain size by using image-processing software (*45*). To obtain the mean grain size, a few regions showing a typical microstructure of the sample (area of ~100 × 100 μm^2 for each) were analyzed. Typically, ~200 grains were measured in a sample. The CPO of olivine in the recovered samples was evaluated by indexing the electron backscattered diffraction (EBSD) patterns using the FE-SEM equipped with an EBSD camera. EBSD patterns were generated via the interaction of a vertical incident electron beam with a polished sample inclined at 70° with respect to the horizontal. The EBSD patterns were indexed using the CHANNEL5 software from HKL Technology. The EBSD pattern of each grain was obtained at 20-kV acceleration voltage and 4-nA probe current. Measurements were performed on a grain-by-grain basis and in operator-controlled indexing mode to obtain an accurate solution. The crystallographic orientation of ~500 grains was measured for each sample. The automatic indexing mode was adopted for the acquisition of crystallographic orientation maps.

Micrometer-scale dislocation microstructures in the deformed samples were evaluated with the FE-SEM using the internal-oxidation dislocation-decoration technique (*46*). Dislocation microstructures of a deformed sample (TO-23) were also investigated by using a JEOL JEM-2010 TEM at 200-kV accelerating voltage. Dark-field images were taken in two-beam conditions, and then the Burgers vector **b**

for the dislocations was determined on the basis of the invisible criteria [that is, $\mathbf{g}\cdot\mathbf{b} = 0$ for screw dislocations; $\mathbf{g}\cdot\mathbf{b} = 0$ and $\mathbf{g}\cdot(\mathbf{b}\times\mathbf{u}) = 0$ for edge dislocations; where $\mathbf{g}$ and $\mathbf{u}$ are the diffraction vector and a unit vector parallel to the dislocation line, respectively]. Thin specimens for TEM observations were prepared from thin sections and then ion-milled with an accelerating voltage of 3 to 5 kV and at a beam angle of 8 to 10°.

The unpolarized infrared absorption spectra of the polycrystalline sample were obtained from the doubly polished sections of the samples (89 to 233 μm thick). The measurements were carried out in dried air by putting the sections on a BaF_2 plate and using a PerkinElmer Spectrum One Fourier transform infrared spectrometer. An aperture size of $50 \times 50\ \mu m^2$ was used for all of the measurements. The absorption peak was hardly observed in dry olivine aggregate samples. The infrared beam was strongly absorbed in the wave numbers ranging from 3500 to 3700 cm^{-1} in wet olivine aggregates (fig. S8). The water content in the olivine in the samples was determined by integrating infrared absorption spectra from 3100 to 3700 cm^{-1} on the basis of the extinction coefficient calibration by Paterson (table S1) (*47*). We calculated the water fugacity from the water content in olivine using a theoretical equation (*48*) and its constants (*49*). The average content of water dissolved in the recovered samples obtained by infrared spectroscopy is summarized in table S1.

SUPPLEMENTARY MATERIALS

Supplementary material for this article is available at http://advances.sciencemag.org/cgi/content/full/1/9/e1500360/DC1

Details on microstructural observations

Fig. S1. Microstructures of the samples.

Fig. S2. Pole figures.

Fig. S3. TEM images.

Fig. S4. Stress-strain records for olivine aggregates.

Fig. S5. The 4–6.5 type cell assembly viewed in cross section.

Fig. S6. Diffraction patterns.

Fig. S7. X-ray radiographs.

Fig. S8. Infrared spectra.

Table S1. Experimental conditions and results.

Table S2. Parameters for the flow laws of olivine aggregates.

Table S3. Flow law parameters of olivine used for the calculation of deformation mechanism maps.

References (*53*, *54*)

REFERENCES AND NOTES

1. S. Karato, P. Wu, Rheology of the upper mantle: A synthesis. *Science* **260**, 771–778 (1993).
2. J. Weertman, J. R. Weertman, High temperature creep of rock and mantle viscosity. *Annu. Rev. Earth Planet. Sci.* **3**, 293–315 (1975).
3. D. L. Kohlstedt, C. Goetze, Low-stress high-temperature creep in olivine single crystals. *J. Geophys. Res.* **79**, 2045–2051 (1974).
4. S. Karato, M. S. Paterson, J. D. FitzGerald, Rheology of synthetic olivine aggregates: Influence of grain size and water. *J. Geophys. Res.* **91**, 8151–8176 (1986).
5. G. Hirth, D. L. Kohlstedt, Experimental constraints on the dynamics of the partially molten upper mantle: 2. Deformation in the dislocation creep regime. *J. Geophys. Res.* **100**, 15441–15449 (1995).
6. T. Hiraga, T. Miyazaki, M. Tasaka, H. Yoshida, Mantle superplasticity and its self-made demise. *Nature* **468**, 1091–1094 (2010).
7. L. N. Hansen, M. E. Zimmerman, D. L. Kohlstedt, Grain boundary sliding in San Carlos olivine: Flow law parameters and crystallographic-preferred orientation. *J. Geophys. Res.* **116**, B08201 (2011).
8. L. N. Hansen, M. E. Zimmerman, A. M. Dillman, D. L. Kohlstedt, Strain localization in olivine aggregates at high temperature: A laboratory comparison of constant-strain-rate and constant-stress boundary conditions. *Earth Planet. Sci. Lett.* **333–334**, 134–145 (2012).
9. B. Evans, C. Goetze, The temperature variation of hardness of olivine and its implication for polycrystalline yield stress. *J. Geophys. Res.* **84**, 5505–5524 (1979).
10. G. Hirth, D. L. Kohlstedt, in *Inside the Subduction Factory*, J. Eiler, Ed. (Geophysical Monograph Series, American Geophysical Union, Washington, DC, 2003), pp. 83–105.
11. S. Mei, D. L. Kohlstedt, Influence of water on plastic deformation of olivine aggregates: 2. Dislocation creep regime. *J. Geophys. Res.* **105**, 21471–21481 (2000).
12. T. Kawazoe, S. Karato, K. Otsuka, Z. Jing, M. Mookherjee, Shear deformation of dry polycrystalline olivine under deep upper mantle conditions using a rotational Drickamer apparatus (RDA). *Phys. Earth Planet. Inter.* **174**, 128–137 (2009).
13. W. B. Durham, S. Mei, D. L. Kohlstedt, L. Wang, N. A. Dixon, New measurements of activation volume in olivine under anhydrous conditions. *Phys. Earth Planet. Inter.* **172**, 67–73 (2009).
14. Y. Nishihara, T. Ohuchi, T. Kawazoe, D. Spengler, M. Tasaka, T. Kikegawa, A. Suzuki, E. Ohtani, Rheology of fine-grained forsterite aggregate at deep upper mantle conditions. *J. Geophys. Res.* **119**, 253–273 (2014).
15. C. Relandeau, High temperature creep of forsterite polycrystalline aggregates. *Geophys. Res. Lett.* **8**, 733–736 (1981).
16. S. Ji, Z. Wang, R. Wirth, Bulk flow strength of forsterite–enstatite composites as a function of forsterite content. *Tectonophysics* **341**, 69–93 (2001).
17. S. Mei, D. L. Kohlstedt, Influence of water on plastic deformation of olivine aggregates: 1. Diffusion creep regime. *J. Geophys. Res.* **105**, 21457–21469 (2000).
18. Y.-H. Zhao, M. E. Zimmerman, D. L. Kohlstedt, Effect of iron content on the creep behavior of olivine: 1. Anhydrous conditions. *Earth Planet. Sci. Lett.* **287**, 229–240 (2009).
19. T. Ohuchi, Y. Nishihara, T. Kawazoe, D. Spengler, R. Shiraishi, A. Suzuki, T. Kikegawa, E. Ohtani, Superplasticity in hydrous melt-bearing dunite: Implications for shear localization in Earth's upper mantle. *Earth Planet. Sci. Lett.* **335–336**, 59–71 (2012).
20. D. L. Kohlstedt, C. Goetze, W. B. Durham, in *The Physics and Chemistry of Minerals and Rocks*, R. G. J. Strens, Ed. (Wiley, New York, 1976), pp. 35–49.
21. S. Karato, S. Zhang, H.-R. Wenk, Superplasticity in Earth's lower mantle: Evidence from seismic anisotropy and rock physics. *Science* **270**, 458–461 (1995).
22. A. Tommasi, D. Mainprice, G. Canova, Y. Chastel, Viscoplastic self-consistent and equilibrium-based modeling of olivine lattice preferred orientations: Implications for the upper mantle seismic anisotropy. *J. Geophys. Res.* **105**, 7893–7908 (2000).
23. H. Jung, I. Katayama, Z. Jiang, T. Hiraga, S. Karato, Effect of water and stress on the lattice-preferred orientation of olivine. *Tectonophysics* **421**, 1–22 (2006).
24. T. G. Langdon, A unified approach to grain boundary sliding in creep and superplasticity. *Acta Metall. Mater.* **42**, 2437–2443 (1994).
25. S. Karato, H. Jung, Effects of pressure on high-temperature dislocation creep in olivine. *Philos. Mag.* **83**, 401–414 (2003).
26. T. Ohuchi, T. Kawazoe, Y. Nishihara, N. Nishiyama, T. Irifune, High pressure and temperature fabric transitions in olivine and variations in upper mantle seismic anisotropy. *Earth Planet. Sci. Lett.* **304**, 55–63 (2011).
27. T. Yoshino, T. Matsuzaki, S. Yamashita, T. Katsura, Hydrous olivine unable to account for conductivity anomaly at the top of the asthenosphere. *Nature* **443**, 973–976 (2006).
28. D. L. Kohlstedt, L. N. Hansen, in *Treatise on Geophysics* (Elsevier, New York, ed. 2, 2015), pp. 441–472.
29. J. X. Mitrovica, A. M. Forte, A new inference of mantle viscosity based upon joint inversion of convection and glacial isostatic adjustment data. *Earth Planet. Sci. Lett.* **225**, 177–189 (2004).
30. G. Kaufmann, K. Lambeck, Glacial isostatic adjustment and the radial viscosity profile from inverse modeling. *J. Geophys. Res.* **107**, ETG 5-1–ETG 5-15 (2002).
31. W. R. Peltier, Postglacial variations in the level of the sea: Implications for climate dynamics and solid-earth geophysics. *Rev. Geophys.* **36**, 603–689 (1998).
32. Y. Ricard, B. Wuming, Inferring the viscosity and the 3-D density structure of the mantle from geoid, topography and plate velocities. *Geophys. J. Int.* **105**, 561–571 (1991).
33. D. Wang, M. Mookherjee, Y. Xu, S. Karato, The effect of water on the electrical conductivity of olivine. *Nature* **443**, 977–980 (2006).
34. C. H. Craig, D. McKenzie, The existence of a thin low-viscosity layer beneath the lithosphere. *Earth Planet. Sci. Lett.* **78**, 420–426 (1986).
35. M. I. Billen, Modeling the dynamics of subducting slabs. *Annu. Rev. Earth Planet. Sci.* **36**, 325–356 (2008).
36. J. van Hunen, S. Zhong, N. M. Shapiro, M. H. Ritzwoller, New evidence for dislocation creep from 3-D geodynamic modeling of the Pacific upper mantle structure. *Earth Planet. Sci. Lett.* **238**, 146–155 (2005).
37. T. E. Tullis, F. G. Horowitz, J. Tullis, Flow laws of polyphase aggregates from end-member flow laws. *J. Geophys. Res.* **96**, 8081–8096 (1991).
38. T. Kawazoe, Y. Nishihara, T. Ohuchi, N. Nishiyama, Y. Higo, K. Funakoshi, T. Irifune, In situ stress-strain measurements in a deformation-DIA apparatus at *P-T* conditions of the upper part of the mantle transition zone. *Am. Mineral.* **96**, 1665–1672 (2011).
39. T. Ohuchi, T. Kawazoe, N. Nishiyama, N. Yu, T. Irifune, Technical development of simple shear deformation experiments using a deformation-DIA apparatus. *J. Earth Sci.* **21**, 523–531 (2010).
40. Y. Seto, Whole pattern fitting for two-dimensional diffraction patterns from polycrystalline materials. *Rev. High Pressure Sci. Technol.* **22**, 144–152 (2012).

41. A. K. Singh, C. Balasingh, H. Mao, R. J. Hemley, J. Shu, Analysis of lattice strains measured under nonhydrostatic pressure. *J. Appl. Phys.* **83**, 7567–7575 (1998).
42. E. H. Abramson, J. M. Brown, L. J. Slutsky, J. Zaug, The elastic constants of San Carlos olivine up to 17 GPa. *J. Geophys. Res.* **102**, 12253–12263 (1997).
43. D. G. Isaak, High-temperature elasticity of iron-bearing olivines. *J. Geophys. Res.* **97**, 1871–1885 (1992).
44. W. Liu, J. Kung, B. Li, Elasticity of San Carlos olivine to 8 GPa and 1073 K. *Geophys. Res. Lett.* **32**, L16301 (2005).
45. T. Ohuchi, A new chemical etching technique for peridotites using molten anhydrous borax. *Am. Mineral.* **91**, 579–583 (2006).
46. S. Karato, Scanning electron microscope observation of dislocations in olivine. *Phys. Chem. Miner.* **14**, 245–248 (1987).
47. M. S. Paterson, The determination of hydroxyl by infrared absorption in quartz, silicate glasses and similar materials. *Bull. Mineral.* **105**, 20–29 (1982).
48. H. Keppler, N. Bolfan-Casanova, Thermodynamics of water solubility and partitioning. *Rev. Mineral. Geochem.* **62**, 193–230 (2006).
49. Y. H. Zhao, S. B. Ginsberg, D. L. Kohlstedt, Solubility of hydrogen in olivine: Dependence on temperature and iron content. *Contrib. Mineral. Petrol.* **147**, 155–161 (2004).
50. J.-C. C. Mercier, Magnitude of the continental lithospheric stresses inferred from rheomorphic petrology. *J. Geophys. Res.* **85**, 6293–6303 (1980).
51. D. McKenzie, J. Jackson, K. Priestley, Thermal structure of oceanic and continental lithosphere. *Earth Planet. Sci. Lett.* **233**, 337–349 (2005).
52. K. Priestley, D. McKenzie, The thermal structure of the lithosphere from shear wave velocities. *Earth Planet. Sci. Lett.* **244**, 285–301 (2006).
53. L. Mehl, B. R. Hacker, G. Hirth, P. B. Kelemen, Arc-parallel flow within the mantle wedge: Evidence from the accreted Talkeetna arc, south central Alaska. *J. Geophys. Res.* **108**, 2375 (2003).
54. P. Phakey, G. Dollinger, J. Christie, in *Flow and Fracture of Rocks*, H. C. Heard, L. Y. Borg, N. L. Carter, C. B. Raleigh, Eds. (Geophysical Monograph Series, American Geophysical Union, Washington, DC, 1972), pp. 117–138.

Acknowledgments: The technical support for the TEM observations given by K. Fujino and the deformation experiments by Y. Nishihara is appreciated. Official reviews by L. N. Hansen and an anonymous reviewer improved the manuscript. **Funding:** This research was conducted with the approval of the Photon Factory Program Advisory Committee (proposal nos. 2010G136 and 2012G133) and SPring-8 (no. 2013B0082), supported by the Grant-in-Aid for Scientific Research (nos. 22340161 and 25707040). **Author contributions:** T.O. conceived the idea, conducted the experiments, and wrote the manuscript. All authors contributed to development of experimental techniques. **Competing interests:** The authors declare that they have no competing interests. **Data and materials availability:** All data associated with this study is in the body of the manuscript and Supplementary Materials.

Submitted 20 March 2015
Accepted 27 August 2015
Published 2 October 2015
10.1126/sciadv.1500360

Citation: T. Ohuchi, T. Kawazoe, Y. Higo, K.-i. Funakoshi, A. Suzuki, T. Kikegawa, T. Irifune, Dislocation-accommodated grain boundary sliding as the major deformation mechanism of olivine in the Earth's upper mantle. *Sci. Adv.* **1**, e1500360 (2015).